CrystEngComm

Cite this: *CrystEngComm*, 2012, **14**, 7764–7770

www.rsc.org/crystengcomm

**PAPER**

# Self-assembled hollow rare earth fluoride alloyed architectures with controlled crystal phase and morphology†

**Zhiming Chen,[ab] Qun Zhao,[a] Guojin Feng,[c] Zhirong Geng[a] and Zhilin Wang*[a]**

***Received 6th February 2012, Accepted 4th May 2012***
**DOI: 10.1039/c2ce25165e**

A general synthetic protocol has been developed to assemble $EuF_3:Ln^{3+}$ and $EuF_3:Ln^{3+}/NH_4^+$ (Ln = Y, Gd, Tb, Dy, Ho, Er, and Tm) alloyed nanocrystallites into hexagon-shaped sub-microcages and hollow sub-microspheres. The structure, morphology and growth kinetics of the alloyed crystallites are investigated. Based on the results obtained by X-ray powder diffraction (XRD), transmission electron microscopy (TEM) and X-ray photoelectron spectra (XPS), it is proposed that the possible formation mechanisms for $EuF_3:Ln^{3+}$ and $EuF_3:Ln^{3+}/NH_4^+$ (Ln = Y, Gd, Tb, Dy, Ho, Er, and Tm) alloyed architectures involves a crystal-phase-mediated self-assembly process. The crystal structure and morphology are strongly influenced by the Eu/Ln feed molar ratio in the starting solution. A higher feed ratio of Eu to Ln facilitates the growth of hexagonal $EuF_3:Ln^{3+}$ (Ln = Y, Gd, Tb, Dy, Ho, Er, and Tm) alloyed crystallites and results in the formation of hexagon-shaped sub-microcages, while a lower feed ratio of Eu to Ln accelerates the growth of cubic $NH_4Ln_3F_{10}:Eu^{3+}$ (Ln = Y, Gd, Tb, Dy, Ho, Er, and Tm) alloyed crystallites and leads to the assembly of the alloyed nanocrystals into hollow sub-microspheres. Additionally, the as-synthesized alloyed architectures show good performance in highly efficient fluorescent host materials.

## Introduction

Shape controlled synthesis and large scale self-assembly of the nanoscale building blocks into hierarchical and complex architectures have been the focus of significant interest in materials chemistry and device fabrications.[1–7] It is expected that if the morphology and assembly mode of the original building units can be controlled, then their secondary architecture would be adjustable to meet different needs. Therefore, the works on morphology-controlled and organization-designed synthesis need to be developed for more novel properties and applications of nanomaterials. To date, many efforts have been made to explore excellent synthetic approaches for the fabrication of metal oxides,[8,9] sulfides,[10–12] hydrates[13–15] and other compounds[16–22] with controlled hierarchical morphologies to enhance their performance in currently existing applications. But due to the complexity of crystal structures and compositions of the materials, it is still a challenging and urgent task for us to control the morphologies of various nano-/micromaterials, consequently achieving a better understanding of the observed complex phenomena of crystal growth and revealing the underlying fundamental theories and principles.

As a category of important functional inorganic materials, rare earth fluorides have been extensively studied and employed in various fields such as optics,[23,24] MALDI matrix,[25] biological labeling and imaging.[26–33] Stimulated by both the promising applications and the interesting properties, much attention has been directed to the controlled synthesis of rare earth fluorides with different sizes and shapes, and the investigation of their morphology-dependent properties in the past several years, especially in rare earth fluoride alloyed nano-/microcrystals.[34–36] Although various rare earth fluoride alloyed nano-/microcrystals have been synthesized in the unintentional result of an attempt to obtain interesting properties,[28–39] there are seldom reports on self-assembly of the alloyed nanocrystals into hollow hierarchical architectures, due to the fact that the synthetic complexity will be increased when more complex product compositions and architectural controls are targeted. However, from the perspective of application, alloyed nanocrystals are not only synthesized in large quantities with desired composition, reproducible size and structure but are also assembled and organized into hierarchical architectures using green and facile methodologies. Furthermore, it is widely documented that hollow structures can provide functional materials with more opportunities for

---

[a] *State Key Laboratory of Coordination Chemistry, School of Chemistry and Chemical Engineering, Nanjing University, Nanjing 210093, People's Republic of China. E-mail: wangzl@nju.edu.cn; Fax: +86-25-83317761; Tel: +86-25-83686082*
[b] *Department of Biochemical Engineering, Anhui Polytechnic University, Wuhu 241000, People's Republic of China*
[c] *Spectrophotometry Laboratory, National Institute of Metrology, Beijing 100013, People's Republic of China*

† Electronic supplementary information (ESI) available: EDX analysis and FT-IR spectrum of $Eu_{0.95}Tb_{0.05}F_3$ hexagon-shaped sub-microcages, the LaMer diagram, SEM and TEM images of $(NH_4)_xEu_{0.75}Tb_{0.25}F_{(3+x)}$ samples, TEM images and XRD patterns of hollow rare earth fluoride alloyed architectures and relevant energy levels and transitions involved in the cross-relaxation and energy-transfer processes in the hollow alloyed architectures. See DOI: 10.1039/c2ce25165e

exploiting novel properties because of their high surface-to-volume ratio and permeability.[40–44] Therefore, the development of a mild and more controlled method for creating alloyed materials with a hollow architecture will be of general interest.

Herein we present an unexpected protocol for the selective synthesis of $EuF_3:Ln^{3+}$ alloyed hexagon-shaped sub-microcages and $EuF_3:Ln^{3+}/NH_4^+$ hollow sub-microspheres (Ln = Y, Gd, Tb, Dy, Ho, Er, and Tm), which involves a crystal-phase-mediated self-assembly process. Our strategy is based on the reactivity difference arousing from the different concentration of $LnF_3$ and $EuF_3$ in aqueous medium. Because the solubility ($K_{sp}$) of $EuF_3$ is close with that of $LnF_3$,[45] the speed of nucleation and growth of alloyed nanocrystals can be controlled by adjusting the feed molar ratio of Eu to Ln in the starting solution. Therefore, the crystal phases and compositions of the alloyed nanocrystallites could be defined, then the self-assembly process and final morphology would be controlled. More important, we also demonstrate that oriented aggregation[46–48] and Ostwald ripening[49,50] can be used as a facile wet chemical route to synthesize alloyed hierarchical architectures with a hollow interior space.

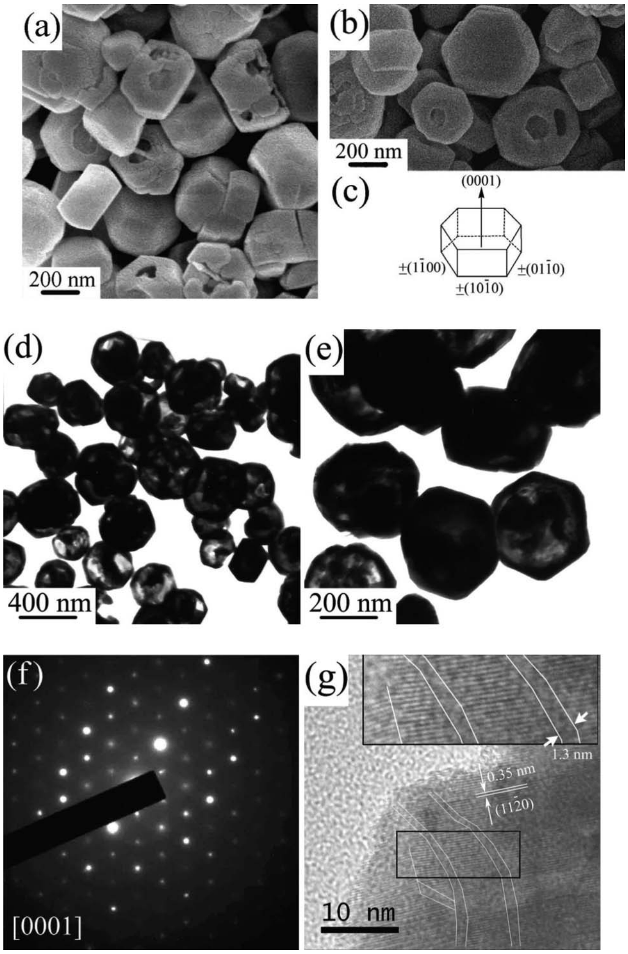

**Fig. 1** (a) and (b) SEM images of $Eu_{0.95}Tb_{0.05}F_3$ hexagon-shaped sub-microcages, (c) schematic diagram showing the anisotropy of $Eu_{0.95}Tb_{0.05}F_3$ hexagon-shaped sub-microcages, (d) and (e) TEM images of $Eu_{0.95}Tb_{0.05}F_3$ hexagon-shaped sub-microcages, (f) SAED pattern for an individual hexagon-shaped sub-microcage oriented along [0001], (g) HRTEM image of an edge region of a sub-microcage (the inset is the magnified image of the selected area).

## Results and discussion

The synthesis of $Eu_{0.95}Tb_{0.05}F_3$ hexagon-shaped sub-microcages has been achieved in 30.5 mL water/ethanol (15.5/15, *v*/*v*) solution containing 0.475 mmol $Eu(NO_3)_3$, 0.025 mmol $Tb(NO_3)_3$ and 5.405 mmol $NH_4F$ by thermal treatment at 110 °C in the presence of 1.71 mmol EDTA for 24 h. Fig. 1a and b show the typical scanning electron microscopy (SEM) images of the as-synthesized hierarchical architectures. These products are usually in hexagonal-prism shapes with an average size of 300 ± 50 nm in length and 440 ± 60 nm in width. Fig. 1d and e show the typical TEM images of the $Eu_{0.95}Tb_{0.05}F_3$ sample, illustrating that these hexagon-shaped sub-microprisms have a hollow interior space. In Fig. 1e, regular hexagonal and rectangular images can be observed, which correspond to hexagon-shaped sub-microcages that are perpendicular and parallel to the copper grids, respectively. The corresponding selected-area electron diffraction (SAED) pattern (Fig. 1f), indicating that the hexagon-shaped sub-microcage is a single crystal, is indexed to the [0001] zone of hexagonal $EuF_3$. Fig. 1g shows the high-resolution TEM (HRTEM) image taken from an edge region of a hexagon-shaped sub-microcage in Fig. 1e, and indicates that the single-crystal hexagon-shaped sub-microcage is constructed from small subunits. It reveals that primary particles attach together with a common crystallographic orientation, and the produced crystals have a layered structure. The interparticle distance is 1–2 nm, suggesting that these nanocrystals assembled in a layer-by-layer stacking style. The 0.35 nm spacing of crystallographic planes corresponds to the $\{11\bar{2}0\}$ lattice fringe of hexagonal $EuF_3$. The XRD pattern (Fig. 2a) indicates that the products are composed of two phases, hexagonal $EuF_3$ ($P\bar{3}c1$, $a$ = 6.920 Å, $c$ = 7.085 Å, JCPDS file no. 32-0373) and orthorhombic $EuF_3$ (*Pnma*, $a$ = 6.619 Å, $b$ = 7.015 Å, $c$ = 4.396 Å, JCPDS file no. 33-0542). Furthermore, energy-dispersive X-ray (EDX) spectroscopy spectrum confirms that the hexagon-shaped microcages are composed of Eu, Tb and F, and the atomic ratio for Eu/Tb/F is near 19/1/60, in agreement with the expected stoichiometry of the $Eu_{0.95}Tb_{0.05}F_3$ crystals (see Fig. S1, ESI†).

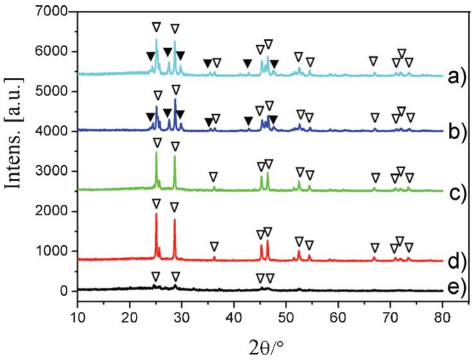

**Fig. 2** XRD patterns for $Eu_{0.95}Tb_{0.05}F_3$ products prepared at 110 °C for (a) 24 h, (b) 15 h, (c) 9 h, (d) 4 h and (e) 1.5 h, respectively. The reflections from the orthorhombic $EuF_3$ are marked by ▼; the reflections from the hexagonal $EuF_3$ are marked by ▽.

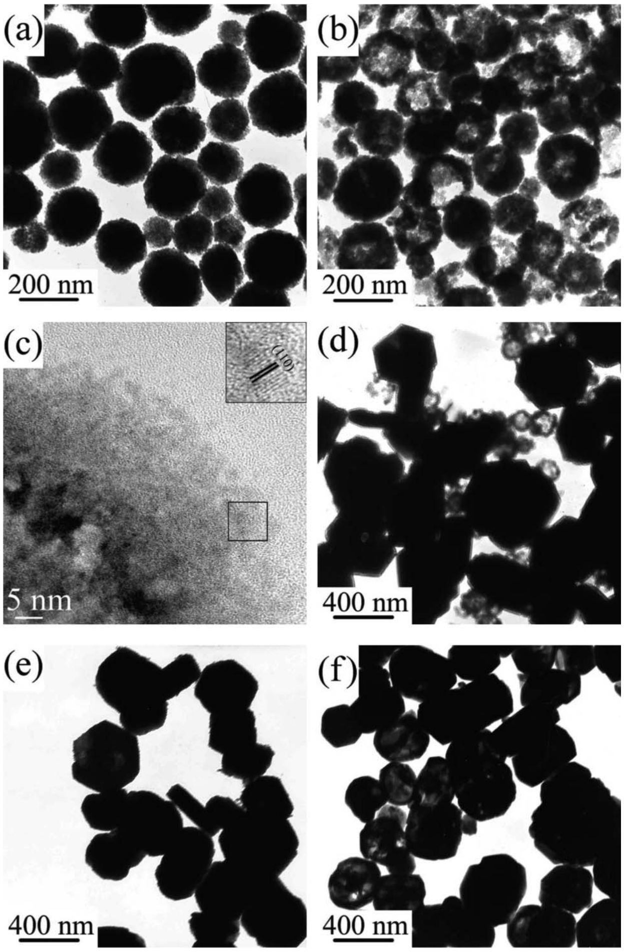

**Fig. 3** TEM images of the samples, showing morphological evolution of $Eu_{0.95}Tb_{0.05}F_3$ hexagon-shaped sub-microcages, obtained in the starting solution with a feed molar ratio of Eu to Tb (19/1, mol/mol), at 110 °C for (a) 1.5 h, (b and c) 4 h, (d) 6 h, (e) 9 h and (f) 15 h, respectively.

To understand the assembling process of $Eu_{0.95}Tb_{0.05}F_3$ hexagon-shaped sub-microcages, the morphology observation and phase identification of the samples isolated at different times were conducted continuously. Fig. 3 is a series of TEM images showing morphological evolution of the hexagon-shaped sub-microcages. With a short reaction time (1.5 h, Fig. 3a), the crystallite aggregates give a spherical morphology. XRD analyses identified them as poorly-crystallized hexagonal $EuF_3$ (Fig. 2e). On the basis of these images, it is understandable that the spherical aggregates underwent a hollowing process when the aging time is prolonged (4 h, Fig. 3b). The HRTEM micrograph (Fig. 3c) of a hollow sub-microsphere in Fig. 3b shows that the shell wall consisted of loosely aggregated nanoparticles, 3 to 5 nm in size, and consequently was highly porous. The clear-cut lattice fringes shown in the HRTEM image of the nanocrystals (inset in Fig. 3c) verify that they are of a high nature of crystallization. Interestingly, these hollow nanospheres can transform into hexagon-shaped sub-microprisms when the aging time is further prolonged (6 h, Fig. 3d). The morphology transformation is much more pronounced after 9 h of the reactive aging (Fig. 3e). The formed hexagon-shaped sub-microprisms are quite uniform with morphological yield of nearly 100%. Also, it is found that during the morphology transformation the structure and crystal phase of the samples do not change. All the XRD peaks can be indexed to the hexagonal phase of $EuF_3$ (Fig. 2c and d). After 15 h hydrothermal treatment, TEM observation confirmed that the hexagon-shaped sub-microprisms underwent another hollowing process (Fig. 3f). XRD results indicated that the products are composed of two kinds of crystal phases (hexagonal and orthorhombic $EuF_3$) (Fig. 2b). It is then understood that the hollowing process was caused by the recrystallization of the alloyed nanocrystallites. Therefore, it is believed that the formation of the hexagon-shaped sub-microcages undergoes four steps in sequence: (1) aggregation of nanocrystallites into spherical aggregates in order to decrease their surface energy; (2) Ostwald ripening process, leading to the formation of the hollow sub-microspheres and uniformed crystalline particles; (3) oriented aggregation process, giving rise to the formation of the hexagon-shaped sub-microprisms; (4) recrystallization process, inducing the formation of $Eu_{0.95}Tb_{0.05}F_3$ hexagon-shaped sub-microcages. It is noteworthy that the hollow spherical aggregates were completely consumed by 9 h hydrothermal treatment, and no hexagon-shaped sub-microprisms were formed within 4 h of the reaction starting. So it is reasonable to suggest that coarsening by conventional Ostwald ripening mechanism of dissolution and growth of pristine particles would first occur before the starting of the oriented aggregation process, which is similar with the formation of single-crystalline $EuF_3$ hexagon-shaped micro-disks.[51]

To investigate the influence of the content of $Tb^{3+}$ ions on the morphological development of the alloyed crystals, we prepared $EuF_3$:$Tb^{3+}$ samples contained various concentration of $Tb^{3+}$ at

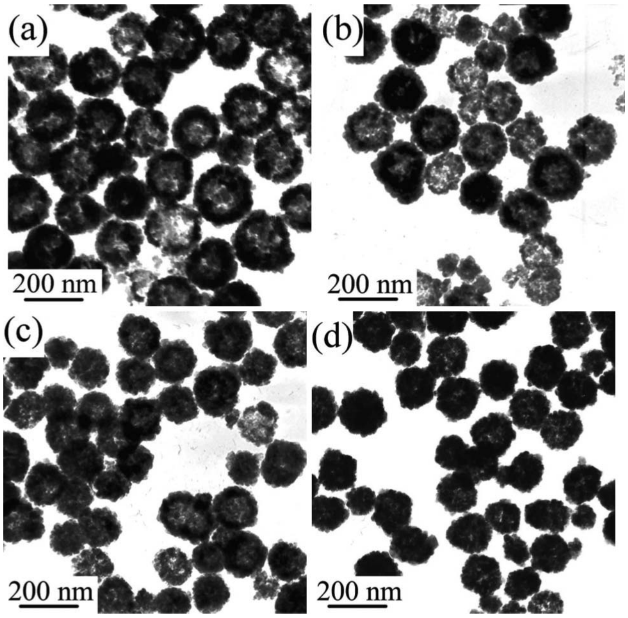

**Fig. 4** TEM images of (a) $(NH_4)_xEu_{0.75}Tb_{0.25}F_{(3+x)}$ hollow sub-microspheres with a diameter of 190 ± 20 nm, (b) $(NH_4)_xEu_{0.6}Tb_{0.4}F_{(3+x)}$ hollow sub-microspheres with a diameter of 170 ± 20 nm, (c) $NH_4Eu_{1.5}Tb_{1.5}F_{10}$ hollow sub-microspheres with a diameter of 150 ± 10 nm, and (d) $NH_4Eu_{0.75}Tb_{2.25}F_{10}$ hollow sub-microspheres with a diameter of 140 ± 10 nm.

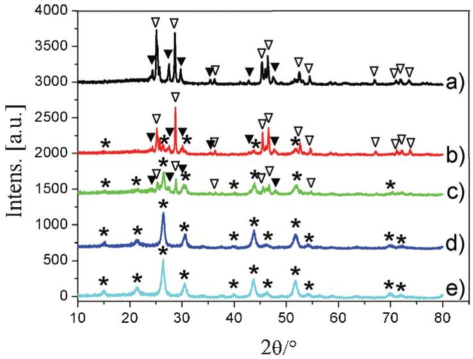

**Fig. 5** XRD patterns of (a) $Eu_{0.95}Tb_{0.05}F_3$ hexagon-shaped sub-microcages, (b) $(NH_4)_xEu_{0.75}Tb_{0.25}F_{(3+x)}$ hollow sub-microspheres, (c) $(NH_4)_xEu_{0.6}Tb_{0.4}F_{(3+x)}$ hollow sub-microspheres, (d) $NH_4Eu_{1.5}Tb_{1.5}F_{10}$ hollow sub-microspheres, (e) $NH_4Eu_{0.75}Tb_{2.25}F_{10}$ hollow sub-microspheres. The reflections from the orthorhombic $EuF_3$ are marked by ▼; the reflections from the hexagonal $EuF_3$ are marked by ▽; the reflections from the cubic $NH_4Tb_3F_{10}$ are marked by *.

110 °C for 24 h. Fig. 4 is a set of TEM images of the alloyed samples prepared in the starting solution with diverse Eu/Tb feed ratios (3/1–1/3). When the sample was prepared with a feed ratio of Eu to Tb at 3/1, hollow sub-microspheres with a diameter about 190 ± 20 nm were obtained (Fig. 4a). The corresponding XRD patterns identified that a third crystal phase was formed, which could be indexed to the cubic $NH_4Tb_3F_{10}$ (Fig. 5b).[52] With the decrease of the Eu/Tb feed ratio to 3/2, the average size of hollow spheres changed to 170 ± 20 nm, accompanying an apparent volume contraction of the inner cavity (Fig. 4b). Correspondingly, the diffraction peaks of $EuF_3$ nanocrystals declined while the reflections of $NH_4Tb_3F_{10}$ increased sharply (Fig. 5c). With a further decrease of the Eu/Tb feed ratio from 1/1 to 1/3, the diameter of the hollow spheres was reduced to a smaller size (145 ± 15 nm, Fig. 4c and d). XRD characterizations show that the reflections of $EuF_3$ nanocrystals completely disappeared. All the peaks of the XRD pattern can be readily indexed to a pure cubic phase of $NH_4Tb_3F_{10}$ (Fig. 5d and e). These observations illustrate that the feed ratio of Eu to Tb is undoubtedly vital in the morphologies and crystallization of the alloyed architectures.

The roles of the feed molar ratio of Eu to Tb in the formation of structure-controlled $EuF_3:Tb^{3+}$ and $EuF_3:Tb^{3+}/NH_4^+$ alloyed nanocrystals can be postulated by applying the LaMer diagram.[53,54] According to the diagram (see Fig. S2, ESI†), the whole particle formation process is divided into three stages: the pre-nucleation stage (Stage I), the nucleation stage (Stage II), and the growth stage (Stage III). When the feed ratio of Eu to Tb is in the range of 19/1–4/1, the $EuF_3$ concentration $C_1$ reaches a maximum concentration for $EuF_3$ nucleation $C_{1\max}$, while the $TbF_3$ concentration $C_2$ is lower than minimum concentration for $TbF_3$ nucleation $C_{2\min}$. So, numerous $EuF_3$ nucleuses (hexagonal phase) were formed rapidly in the nucleation stage. Subsequently, $Eu_xTb_{(1-x)}F_3$ was grown on these $EuF_3$ nucleuses in the growth stage. As a result, uniform hexagonal phases of $Eu_xTb_{(1-x)}F_3$ alloyed crystalline were formed. When the feed ratio of Eu to Tb is in the range of 1/1–1/3, the $EuF_3$ concentration $C_1$ is lower than $C_{1\min}$, while the $TbF_3$ concentration $C_2$ is in the range of $C_{2\min}$–$C_{2\max}$. So, numerous $TbF_3$ clusters were formed and grown in the nucleation stage. Because $NH_4^+$ can be incorporated into the framework of Tb–F,[53,54] the formed nucleuses are cubic $NH_4Tb_3F_{10}$. Subsequently, $NH_4Eu_xTb_{(3-x)}F_{10}$ was grown on the $NH_4Tb_3F_{10}$ nucleuses in the growth stage. As a result, cubic $NH_4Tb_3F_{10}:Eu^{3+}$ alloyed crystalline were obtained. If the feed ratio of Eu to Tb is in the range of 3/1–1/1, the resultant concentrations of $EuF_3$ and $TbF_3$ are in the range of $C_{\min}$–$C_{\max}$. So, both $EuF_3$ and $NH_4Tb_3F_{10}$ nucleuses were formed and grown in the nucleation stage. In the growth stage, $EuF_3$ and $NH_4Tb_3F_{10}$ were grown on these $EuF_3$ and $NH_4Tb_3F_{10}$ nucleuses, respectively, and resulted in the formation of mixture phases of the alloyed crystals. As mentioned above, only uniform crystalline particles can be assembled into organized conformations and geometrical architectures. It is understandable that $Eu_xTb_{(1-x)}F_3$ hexagon-shaped sub-microcages were only formed in a higher feed ratio of Eu to Tb solution (19/1–4/1).

To confirm this hypothesis, we investigated the chemical composition of $EuF_3:Tb^{3+}$ and $EuF_3:Tb^{3+}/NH_4^+$ alloyed samples. Fig. 6 depicts the typical XPS survey spectra of $EuF_3:Tb^{3+}$ and $EuF_3:Tb^{3+}/NH_4^+$ samples contained various amounts of $Tb^{3+}$ (5, 25, 40, and 50%). In agreement with the XRD results, pointing out the formation of cubic phases of $NH_4Tb_3F_{10}:Eu^{3+}$ upon increasing the $Tb^{3+}$ content, XPS analysis evidenced a progressive increase of the nitrogen content in the alloyed samples. Compared to the $Eu_{0.95}Tb_{0.05}F_3$ sample (curve a), the peaks of the Eu $3d_{5/2}$ spectrum for the samples with a high $Tb^{3+}$ content show a small negative shift, which suggests the difference of the complexation state and the crystal field of the fluoride matrix. Since the bonds of Ln–F in $LnF_3$ are different with those of $NH_4Ln_3F_{10}$,[55–59] the small negative shift of Eu $3d_{5/2}$ can be indexed to the more electron cloud drain from the $Eu^{3+}$ to $F^-$ due to the shorter bonds of Eu–F. Consistent with this, the Tb $3d_{5/2}$ spectrum of the samples with a high Eu content reveals a negative shift toward lower binding energy compared to those of the $NH_4Eu_{1.5}Tb_{1.5}F_{10}$ sample (curve d). Further evidences were draw from the F 1s spectra. The peak at 683.8 eV is assigned to Ln–F of $EuF_3:Tb^{3+}$, while the peak located at 683.3 eV could be

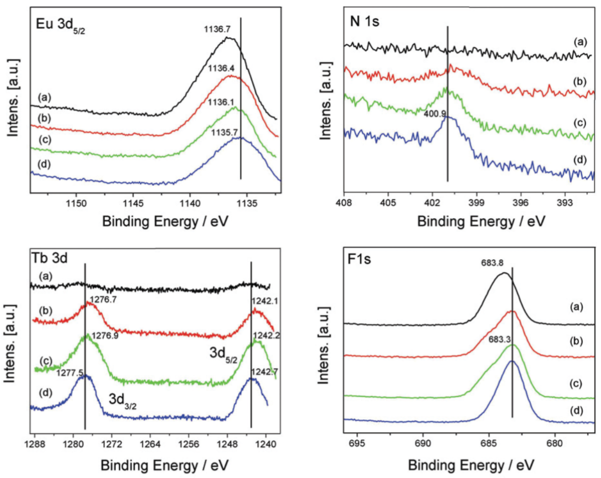

**Fig. 6** XPS spectra of Eu, Tb, N, and F for (a) $Eu_{0.95}Tb_{0.05}F_3$ hexagon-shaped sub-microcages, (b) $(NH_4)_xEu_{0.75}Tb_{0.25}F_{(3+x)}$ hollow sub-microspheres, (c) $(NH_4)_xEu_{0.6}Tb_{0.4}F_{(3+x)}$ hollow sub-microspheres, (d) $NH_4Eu_{1.5}Tb_{1.5}F_{10}$ hollow sub-microspheres.

attributed to Ln–F of $NH_4Tb_3F_{10}$:$Eu^{3+}$.[60–62] With the increase of $Tb^{3+}$ content, the peak intensity of 683.3 eV increased, suggesting that the hexagonal phase of $EuF_3$:$Tb^{3+}$ crystals were formed in the solution with a higher feed ratio of Eu to Tb. According to the above hypothesis, no $EuF_3$ nucleuses was formed in the solution with a lower feed ratio of Eu to Tb (1/1–1/3). As expected, the peak at 683.8 eV is no longer observed in sample d, confirming that there is no hexagonal phase of $EuF_3$:$Tb^{3+}$ crystal in this product. Based on these evidences, it is reasonable to conclude that the formation process of the controlled alloyed crystal was fitted to the LaMer diagram.

Formation of the $Eu_{0.95}Tb_{0.05}F_3$ alloyed hollow architectures can now be further addressed. As depicted in Scheme 1a, the sphere formation and related hollowing can be explained by an Ostwald ripening process (step 1), while the formation of a hexagon-shaped sub-microcage can be ascribed to a cooperation of oriented aggregation and recrystallization processes. Since EDTA anions are adsorbed on the surface of $Eu_xTb_{(1-x)}F_3$ alloyed crystals (see Fig. S3, ESI†), the outer negativity layer can serve as a diffusion boundary to restrain rapid crystal growth and prevent direct fusion among the pristine particles during the coarsening process. Therefore, the epitaxial growth of the alloyed crystal was suppressed, and the size of the alloyed crystals was maintained. To decrease the total surface energy, the adjacent crystallites of the sub-microspheres re-assembled to share a common crystallographic orientation, inducing the formation of hexagon-shaped sub-microprisms. This kind of re-arrangement is an irreversible process. After all the hollow sub-microspheres were converted into hexagon-shaped sub-microprisms, the crystallites located in the inner part of the hexagon-shaped sub-microprisms would be dissolved and re-deposited on the outer parts, resulting in the creation of the hexagon-shaped sub-microcages. This hypothesis had been confirmed by continuously monitoring the morphological evolution of the hexagon-shaped sub-microcages (see Fig. 3). In contrast, under similar processing conditions, the obtained $EuF_3$:$Tb^{3+}$/$NH_4^+$ alloyed architectures are hollow sub-microspheres when the $Tb^{3+}$ concentration is increased to 25–75%. This observation indicates that these hollow sub-microspheres underwent a different formation process (Scheme 1b). With the increase of $Tb^{3+}$ content, the organizing structures of the pristine nanocrystallites in the solid aggregates vary with compositional changes in the synthesis. The outer $NH_4Tb_3F_{10}$:$Eu^{3+}$ layer neither restrains rapid crystal growth nor prevents direct fusion among the pristine particles. In this connection, it is conceivable that no $EuF_3$:$Tb^{3+}$/$NH_4^+$ hollow sub-microsphere can convert to hexagon-shaped sub-microprisms. This consequence has been confirmed by monitoring the ripening process of $(NH_4)_xEu_{0.75}Tb_{0.25}F_{(3+x)}$ crystals (see Fig. S4, ESI†), in which the size of the alloyed nanocrystal is enlarging in the ripening process.

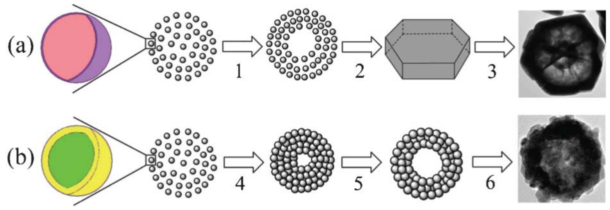

**Scheme 1** (a) Formation process of $Eu_{0.95}Tb_{0.05}F_3$ alloyed hexagon-shaped sub-microcages: coarsening of the alloyed crystals *via* Ostwald ripening (1), construction of hexagon-shaped sub-microcages by a cooperation of an oriented aggregation and recrystallization processes (2, 3). (b) Formation process of $EuF_3$:$Tb^{3+}$/$NH_4^+$ alloyed hollow sub-microspheres *via* Ostwald ripening process (4–6). The pink section illustrates the $EuF_3$ core, the purple section illustrates the $Eu_xTb_{(1-x)}F_3$ shell; the green section illustrates the $NH_4Tb_3F_{10}$ core, the yellow section illustrates the $NH_4Tb_3F_{10}$:$Eu^{3+}$ shell.

This protocol can be further extended to produce $EuF_3$:$Ln^{3+}$ and $EuF_3$:$Ln^{3+}$/$NH_4^+$ (Ln = Y, Gd, Dy, Ho, Er, and Tm) alloyed hexagon-shaped sub-microcages and hollow sub-microspheres (see Fig. S5–S7, ESI†). Similar crystal structures and self-assembly processes have been observed in these alloyed crystals. With the same concentration of $Eu^{3+}$ ions, hollow sub-microspheres with obvious smaller sizes have been observed in the samples of $EuF_3$:$Ln^{3+}$/$NH_4^+$ (Ln = Y, Ho, Er, and Tm). Our XRD investigations show that the cubic phase of $NH_4Ln_3F_{10}$:$Eu^{3+}$ (Ln = Y, Ho, Er, and Tm) nanocrystals were formed more easily in these samples, perhaps due to the contraction of the ionic radii of $Ln^{3+}$.

The luminescence of lanthanide ions mainly arises from the 4f electrons, which is highly sensitive to the composition and structure of the host materials.[24] To investigate the influence of the $Tb^{3+}$ dopant on the emission behaviour of $Eu^{3+}$, we characterized the luminescent capabilities of $EuF_3$:$Tb^{3+}$ and $EuF_3$:$Tb^{3+}$/$NH_4^+$ hollow sub-microstructures at room temperature. In general, under 350–420 nm and 330–390 nm UV excitation, $Eu^{3+}$ and $Tb^{3+}$-doped compounds emit red and bright green fluorescence with a narrow emission spectrum, respectively. In the case of $EuF_3$:$Tb^{3+}$ and $EuF_3$:$Tb^{3+}$/$NH_4^+$ alloyed crystals, when excited by ordinary Xe sources, these phosphors emit strong and red fluorescence. Fig. 7a and b show the excitation and emission spectra for the hexagon-shaped sub-microcages and hollow sub-microspheres. It can be seen clearly that the excitation spectra exhibit some differences depending on the concentration of $Tb^{3+}$ in the alloyed crystals. Increasing the content of $Tb^{3+}$ induces a blue shift of the excitation (Fig. 7a). Significantly, under 379 nm UV excitation, the obtained emission spectra exhibit characteristic lines of $Eu^{3+}$, and no emission from $Tb^{3+}$ is observed, indicating that an efficient energy transfer occurs from $Tb^{3+}$ to $Eu^{3+}$ in these phosphors. Although the luminescent positions of these alloyed samples are identical, the luminescent intensity is much different. With an increase of $Tb^{3+}$ content in the alloyed crystals, the luminescence of $Eu^{3+}$ is the competitive result of a ternary of effects. First, the increase of $Tb^{3+}$ content decreases the concentration of luminescent centres, which is evidenced by the continual decrease of the emission intensity of $Eu^{3+}$ (Fig. 7b, curve 1–3). Second, the increase of $Tb^{3+}$ content enhances the probability of energy transfer from $Tb^{3+}$ to $Eu^{3+}$. Also, the increase of $Tb^{3+}$ content decreases the probability of non-radiative energy migration between $Eu^{3+}$ ions up to quenching centers, where the excitation energy is lost non-radiatively. These are confirmed by the special emission intensity and lifetime of $Eu^{3+}$ in $NH_4Eu_{0.75}Tb_{2.25}F_{10}$ hollow sub-microspheres. As shown in Fig. 7c, $NH_4Eu_{1.5}Tb_{1.5}F_{10}$ hollow sub-microspheres exhibits the fastest fluorescent decay of the 592 nm emission of $Eu^{3+}$ (3.84 ms, $Eu_{0.95}Tb_{0.05}F_3$ hexagon-shaped sub-microcages; 1.78 ms, $(NH_4)_xEu_{0.75}Tb_{0.25}F_{(3+x)}$ hollow sub-microspheres; 1.15 ms, $NH_4Eu_{1.5}Tb_{1.5}F_{10}$ hollow sub-microspheres; 2.08 ms, $NH_4Eu_{0.75}Tb_{2.25}F_{10}$ hollow sub-microspheres).

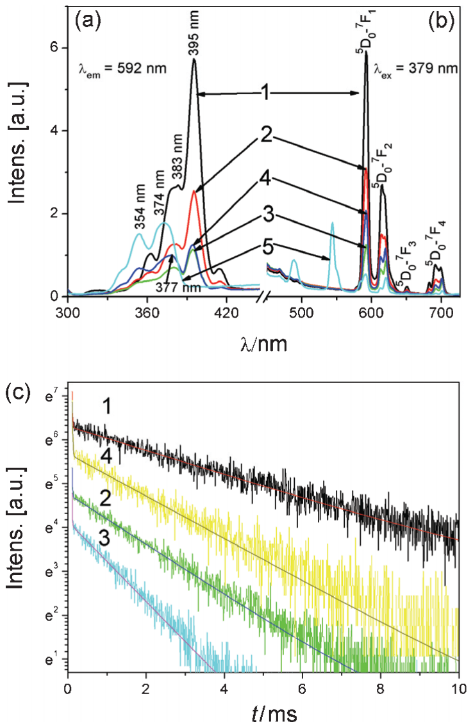

**Fig. 7** (a) Excitation spectra ($\lambda_{em}$ = 592 nm), (b) emission spectra ($\lambda_{ex}$ = 379 nm) and (c) luminescence decay curves of the 592 nm emission of $Eu^{3+}$ ions ($\lambda_{ex}$ = 379 nm) of (1) $Eu_{0.95}Tb_{0.05}F_3$ hexagon-shaped sub-microcages, (2) $(NH_4)_xEu_{0.75}Tb_{0.25}F_{(3+x)}$ hollow sub-microspheres, (3) $NH_4Eu_{1.5}Tb_{1.5}F_{10}$ hollow sub-microspheres, (4) $NH_4Eu_{0.75}Tb_{2.25}F_{10}$ hollow sub-microspheres and (5) $NH_4Tb_3F_{10}$ sample obtained by reaction of $Tb(NO_3)_3$ and $NH_4F$ in the similar synthetic system.

Similar luminescence properties have been observed in $EuF_3$:$Ln^{3+}$ and $EuF_3$:$Ln^{3+}$/$NH_4^+$ (Ln = Y and Gd) alloyed crystals. However, the characteristic emissions of $Eu^{3+}$ originating from the transitions from the excited $^5D_0$ to the ground states $^7F_j$ ($j$ = 1–4) were completely quenched by a low content of dopant ions ($Dy^{3+}$, $Ho^{3+}$, $Er^{3+}$ or $Tm^{3+}$), perhaps due to an efficient energy transfer from $Eu^{3+}$ to $Ln^{3+}$ (Ln = $Dy^{3+}$, $Ho^{3+}$, $Er^{3+}$, and $Tm^{3+}$).[63] In these energy transfers, the $^4F_{9/2}$ state of $Dy^{3+}$, the $^5F_5$ state of $Ho^{3+}$, the $^4I_{13}$ state of $Er^{3+}$ and the $^3F_4$ state of $Tm^{3+}$ acceptor ions are present to act as acceptors for the excitation energy of the $Eu^{3+}$ ($^5D_1$, $^5D_2$) donor state, separately (see Fig. S8, ESI†).

## Conclusions

In this work, a general synthetic method has been developed to assemble $EuF_3$:$Ln^{3+}$ and $EuF_3$:$Ln^{3+}$/$NH_4^+$ (Ln = Y, Gd, Tb, Dy, Ho, Er, and Tm) alloyed nanocrystallites into hexagon-shaped sub-microcages and hollow sub-microspheres, which have merits of one-step, mass production, and easy operation. The crystal phases of the alloyed nanocrystallites can be defined, then the self-assembly process and final morphology would be controlled. The time-dependent experiments revealed a multi-step organization process, in which hollow sub-microspheres of $Eu_{0.95}Tb_{0.05}F_3$ were formed first due to the Ostwald ripening and then reorganized into hexagon-shaped sub-microprisms by an oriented aggregation process; the subsequent hollowing process resulted in the formation of the final hexagon-shaped sub-microcages. XRD and XPS analyses indicate that the nucleation and growth of $EuF_3$:$Ln^{3+}$ and $EuF_3$:$Ln^{3+}$/$NH_4^+$ (Ln = Y, Gd, Tb, Dy, Ho, Er, and Tm) alloyed crystals were under kinetic control. Luminescence spectra and decay curves show that the optical properties of the hollow architectures are relevant to their various product compositions, morphology and crystal structure. This work offers a new strategy to design the crystal phase of alloyed materials and provides a novel approach for hierarchical assembly of hollow architectures according to different application purposes.

## Experimental

All chemicals and reagents were analytical grade, purchased from Sinopharm Chemical Reagent Co. Ltd. (Shanghai, China), and used as received without further purification. The water used throughout the experiment was prepared from a Milli-Q water purification system (Millipore, Milford, MA). In the typical synthesis, ethylenediaminetetraacetic acid (EDTA) solution was obtained by dissolving 500 mg of EDTA in 6.5 mL of 1 M ammonium hydroxide solution. $NH_4F$ solution was obtained by dissolving 200 mg of $NH_4F$ in 7 mL of water/ethanol (2/5, $v$/$v$). Mixed $Eu_2O_3$ and rare earth oxides with designated mole ratio (0.5 mmol in total) was completely dissolved in 7 mL of 0.71 M $HNO_3$ to form $Eu(NO)_3$ and $Ln(NO)_3$ solution. Then, the EDTA solution and 10 mL of ethanol were added to the obtained $Eu(NO)_3$ and $Ln(NO)_3$ solution in sequence. After a 5 min ultrasonic bath, the $NH_4F$ solution was introduced. Subsequently, the mixed system was sonicated for 5 min to ensure homogeneous dispersion of all reagents in the solutions and transferred into a Teflon-lined autoclave. After the autoclave was tightly sealed and heated at 110 °C for 4–24 h and the system was allowed to cool to room temperature naturally. The as-obtained precipitate was collected, washed with distilled water and absolute ethanol several times, and finally dried at 110 °C in air for 0.5 h.

XRD analyses were performed on a Shimadzu XRD-6000 X-ray diffractometer with Cu-Ka radiation ($\lambda$ = 0.15406 nm) at a scanning rate of 0.1° $s^{-1}$ in the $2\theta$ range from 20 to 80°. The morphologies and compositions of the products were characterized by a JEM-200CX transmission electron microscope, a Hitachi S-4800 scanning electron microscope and a JEM 2010 high-resolution transmission electron microscope with an energy-dispersive X-ray spectroscope. The XPS spectra were acquired on Thermo Scientific K-Alpha equipment equipped with an aluminum anode monochromatic source (1486.6 eV). The binding energies (BEs) of XPS spectra of all studied elements were referred to the C 1s photoelectron peak arising from adventitious carbon (*i.e.* BE of C 1s was set at 284.6 eV). Fourier transform infrared spectrum (FT-IR) was obtained on a Vector$^{TM}$ 22. Luminescent spectra were carried out on an Aminco Bowman luminescence spectrometer equipped with a 150 W Xe arc lamp at room temperature. The luminescence lifetime of $Eu^{3+}$ was measured using an Edinburgh Instruments' FLS 920 instrument with a Pulsed Xenon Microsecond Flash Lamp (μF900) and a red sensitive R928-P (185–870 nm). All lifetime analyses were calculated using the Edinburgh Instruments F900 software and signal intensities greater than

1% of the maximum intensity were included, and were fitted so as to obtain c2 values from 1.0 to 1.3.

## Acknowledgements

This work was supported by the National Natural Science Foundation of China (21075064, 21027013, 21021062, 21101002 and 90813020) and the National Basic Research Program of China (2007CB925102).

## References

1 I. Bita, J. K. W. Yang, Y. S. Jung, C. A. Ross, E. L. Thomas and K. K. Berggren, *Science*, 2008, **321**, 939–943.
2 J. Y. Cheng, A. M. Mayes and C. A. Ross, *Nat. Mater.*, 2004, **3**, 823–828.
3 H. Cölfen and S. Mann, *Angew. Chem., Int. Ed.*, 2003, **42**, 2350–2365.
4 H. Cölfen and M. Antonietti, *Angew. Chem., Int. Ed.*, 2005, **44**, 5576–5591.
5 J. A. A. W. Elemans, A. E. Rowan and R. J. M. Nolte, *J. Mater. Chem.*, 2003, **13**, 2661–2670.
6 S. A. Jenekhe and X. L. Chen, *Science*, 1999, **283**, 372–375.
7 D. Wouters, S. Hoeppener and U. S. Schubert, *Angew. Chem., Int. Ed.*, 2009, **48**, 1732–1739.
8 D. B. Kuang, B. X. Lei, Y. P. Pan, X. Y. Yu and C. Y. Su, *J. Phys. Chem. C*, 2009, **113**, 5508–5513.
9 X. F. Song and L. Gao, *J. Phys. Chem. C*, 2008, **112**, 15299–15305.
10 Y. W. Jun, S. M. Lee, N. J. Kang and J. Cheon, *J. Am. Chem. Soc.*, 2001, **123**, 5150–5151.
11 F. Gao, Q. Y. Lu, S. H. Xie and D. Y. Zhao, *Adv. Mater.*, 2002, **14**, 1537–1540.
12 X. Y. Chen, X. Wang, Z. H. Wang, X. G. Yang and Y. T. Qian, *Cryst. Growth Des.*, 2005, **5**, 347–350.
13 Z. P. Zhang, X. Q. Shao, H. D. Yu, Y. B. Wang and M. Y. Han, *Chem. Mater.*, 2005, **17**, 332–336.
14 M. H. Cao, X. Y. He, J. Chen and C. W. Hu, *Cryst. Growth Des.*, 2007, **7**, 170–174.
15 L. X. Yang, Y. J. Zhu, L. Li, L. Zhang, H. Tong, W. W. Wang, G. F. Cheng and J. F. Zhu, *Eur. J. Inorg. Chem.*, 2006, 4787–4792.
16 S. H. Yu, M. Antonietti, H. Cölfen and J. Hartmann, *Nano Lett.*, 2003, **3**, 379–382.
17 Q. Gong, X. F. Qian, X. D. Ma and Z. K. Zhu, *Cryst. Growth Des.*, 2006, **6**, 1821–1825.
18 L. H. Lu, R. Capek, A. Kornowski, N. Gaponik and A. Eychmüller, *Angew. Chem., Int. Ed.*, 2005, **44**, 5997–6001.
19 T. X. Wang, M. Antonietti and H. Cölfen, *Chem.–Eur. J.*, 2006, **12**, 5722–5730.
20 J. H. Zhu, S. H. Yu, A. W. Xu and H. Cölfen, *Chem. Commun.*, 2009, 1106–1108.
21 F. Zhang, Y. F. Shi, X. H. Sun, D. Y. Zhao and G. D. Stucky, *Chem. Mater.*, 2009, **21**, 5237–5243.
22 W. Feng, L. D. Sun, Y. W. Zhang and C. H. Yan, *Small*, 2009, **5**, 2057–2060.
23 X. Wang, J. Zhuang, Q. Peng and Y. D. Li, *Inorg. Chem.*, 2006, **45**, 6661–6665.
24 J. W. Stouwdam and F. C. J. M. van Veggel, *Nano Lett.*, 2002, **2**, 733–737.
25 Z. M. Chen, Z. R. Geng, D. L. Shao, Y. H. Mei and Z. L. Wang, *Anal. Chem.*, 2009, **81**, 7625–7631.
26 G. S. Yi, H. C. Lu, S. Y. Zhao, Y. Ge, W. J. Yang, D. P. Chen and L. H. Guo, *Nano Lett.*, 2004, **4**, 2191–2196.
27 H. C. Lu, G. S. Yi, S. Y. Zhao, D. P. Chen, L. H. Guo and J. Cheng, *J. Mater. Chem.*, 2004, **14**, 1336–1341.
28 S. Sivakumar, P. R. Diamente, F. C. J. van Veggel and M. Raudsepp, *Chem.–Eur. J.*, 2006, **12**, 5878–5884.
29 L. Y. Wang, R. X. Yan, Z. Y. Huo, L. Wang, J. H. Zeng, J. Bao, X. Wang, Q. Peng and Y. D. Li, *Angew. Chem., Int. Ed.*, 2005, **44**, 6054–6057.
30 F. Wang and X. G. Liu, *Chem. Soc. Rev.*, 2009, **38**, 976–989.
31 M. Haase and H. Schäfer, *Angew. Chem., Int. Ed.*, 2011, **50**, 5808–5829.
32 F. Wang, D. Banerjee, Y. S. Liu, X. Y. Chen and X. G. Liu, *Analyst*, 2010, **135**, 1839–1854.
33 G. F. Wang, Q. Peng and Y. D. Li, *Acc. Chem. Res.*, 2011, **44**, 322–332.
34 M. M. Lezhnina, T. Jüstel, H. Kätker, D. U. Wiechert and U. H. Kynast, *Adv. Funct. Mater.*, 2006, **16**, 935–942.
35 C. H. Dong and F. C. J. M. van Veggel, *ACS Nano*, 2009, **3**, 123–130.
36 Z. L. Wang, Z. W. Quan, P. Y. Jia, C. K. Lin, Y. Luo, Y. Chen, J. Fang, W. Zhou, C. J. O'Connor and J. Lin, *Chem. Mater.*, 2006, **18**, 2030–2037.
37 C. X. Li, Z. W. Quan, P. P. Yang, S. S. Huang, H. Z. Lian and J. Lin, *J. Phys. Chem. C*, 2008, **112**, 13395–13404.
38 C. X. Li, J. Yang, P. P. Yang, H. Z. Lian and J. Lin, *Chem. Mater.*, 2008, **20**, 4317–4326.
39 L. Y. Wang and Y. D. Li, *Chem. Mater.*, 2007, **19**, 727–734.
40 K. Kamata, Y. Lu and Y. N. Xia, *J. Am. Chem. Soc.*, 2003, **125**, 2384–2385.
41 Y. Hu, J. F. Chen, W. M. Chen, X. H. Lin and X. L. Li, *Adv. Mater.*, 2003, **15**, 726–729.
42 H. G. Yang and H. C. Zeng, *Angew. Chem., Int. Ed.*, 2004, **43**, 5206–5209.
43 Q. Peng, Y. J. Dong and Y. D. Li, *Angew. Chem., Int. Ed.*, 2003, **42**, 3027–3030.
44 X. W. Lou, Y. Wang, C. L. Yuan, J. Y. Lee and L. A. Archer, *Adv. Mater.*, 2006, **18**, 2325–2329.
45 C. H. Huang, *Coordination Chemistry of Rare Earth Elements*, Science Publishing Press, Beijing, 1997, **ch. 2**, p. 29.
46 R. L. Penn and J. F. Banfield, *Science*, 1998, **281**, 969–971.
47 H. G. Yang and H. C. Zeng, *Angew. Chem., Int. Ed.*, 2004, **43**, 5930–5933.
48 B. Liu and H. C. Zeng, *J. Am. Chem. Soc.*, 2004, **126**, 8124–8125.
49 J. Li and H. C. Zeng, *Angew. Chem., Int. Ed.*, 2005, **44**, 4342–4345.
50 B. Liu and H. C. Zeng, *Small*, 2005, **1**, 566–571.
51 Z. M. Chen, Z. R. Geng, M. L. Shi, Z. H. Liu and Z. L. Wang, *CrystEngComm*, 2009, **11**, 1591–1596.
52 X. Liang, X. Wang, L. Y. Wang, R. X. Yan, Q. Peng and Y. D. Li, *Eur. J. Inorg. Chem.*, 2006, 2186–2191.
53 V. K. LaMer and R. H. Dinegar, *J. Am. Chem. Soc.*, 1950, **72**, 4847–4854.
54 T. Sugimoto, *Adv. Colloid Interface Sci.*, 1987, **28**, 65–108.
55 Z. J. Kang, Y. X. Wang, F. T. You and J. H. Lin, *J. Solid State Chem.*, 2001, **158**, 358–362.
56 S. P. Sinha, *Struct. Bonding*, 1976, **25**, 69–149.
57 V. F. Zinchenko, N. P. Efryushina, O. G. Eryomin, V.Ya. Markiv, N. M. Belyavina, O. V. Mozkova and M. I. Zakharenko, *J. Alloys Compd.*, 2002, **347**, L1–L3.
58 A. Zalkin and D. H. Templeton, *Acta Crystallogr., Sect. B: Struct. Sci.*, 1985, **41**, 91–93.
59 A. Arbus, M. T. Fournier, B. Picaud, G. Boulon and A. Vedrine, *J. Solid State Chem.*, 1980, **31**, 11–21.
60 Y. P. Du, Y. W. Zhang, L. D. Sun and C. H. Yan, *J. Phys. Chem. C*, 2008, **112**, 405–415.
61 R. Vercaemst, D. Poelman, L. Fiermans, R. L. Van Meirhaeghe, W. H. Laflère and F. Cardon, *J. Electron Spectrosc. Relat. Phenom.*, 1995, **74**, 45–56.
62 H. S. Qian and Y. Zhang, *Langmuir*, 2008, **24**, 12123–12125.
63 J. R. Lakowicz, *Principles of Fluorescence Spectroscopy (3rd Edition)*, Springer, 2006, **ch. 13**, p. 433–467.